

## Article

# The Research on Deep Learning-Driven Dimensionality Reduction and Strain Prediction Techniques Based on Flight Parameter Data

Wenbo Huang <sup>1</sup>, Rui Wang <sup>2</sup> , Mengchuang Zhang <sup>2,3,\*</sup>  and Zhiping Yin <sup>2,\*</sup><sup>1</sup> Shanghai Aircraft Design and Research Institute of COMAC, Shanghai 200232, China; huangwenbo@comac.cc<sup>2</sup> School of Civil Aviation, Northwestern Polytechnical University, Xi'an 710072, China; wr650012@163.com<sup>3</sup> Shenzhen Research Institute of Northwestern Polytechnical University, Shenzhen 518057, China

\* Correspondence: mczhang@nwpu.edu.cn (M.Z.); yinzhiping\_nwpu@163.com (Z.Y.)

**Abstract:** Loads and strains in critical areas play a crucial role in aircraft structural health monitoring, the tracking of individual aircraft lifespans, and the compilation of load spectra. Direct measurement of actual flight loads presents challenges. This process typically involves using load-strain stiffness matrices, derived from ground calibration tests, to map measured flight parameters to loads at critical locations. Presently, deep learning neural network methods are rapidly developing, offering new perspectives for this task. This paper explores the potential of deep learning models in predicting flight parameter loads and strains, integrating the methods of flight parameter preprocessing techniques, flight maneuver recognition (FMR), virtual ground calibration tests for wings, dimensionality reduction of flight data through Autoencoder (AE) network models, and the application of Long Short-Term Memory (LSTM) network models to predict strains. These efforts contribute to the prediction of strains in critical areas based on flight parameters, thereby enabling real-time assessment of aircraft damage.

**Keywords:** maneuver flight recognition (MFR); autoencoder (AE) neural network; flight parameter dimensionality reduction; long short-term memory neural network (LSTM); strain prediction



**Citation:** Huang, W.; Wang, R.; Zhang, M.; Yin, Z. The Research on Deep Learning-Driven Dimensionality Reduction and Strain Prediction Techniques Based on Flight Parameter Data. *Appl. Sci.* **2024**, *14*, 3938. <https://doi.org/10.3390/app14093938>

Academic Editor: Jérôme Morio

Received: 24 March 2024

Revised: 27 April 2024

Accepted: 30 April 2024

Published: 5 May 2024



**Copyright:** © 2024 by the authors. Licensee MDPI, Basel, Switzerland. This article is an open access article distributed under the terms and conditions of the Creative Commons Attribution (CC BY) license (<https://creativecommons.org/licenses/by/4.0/>).

## 1. Introduction

As performance requirements for aircraft continue to escalate, the structures of these aircraft are subjected to increasingly extreme mechanical environments [1]. Consequently, the structural health monitoring and maintenance of aircraft are of critical importance. Currently, structural health monitoring mainly focuses on the wings and key areas associated with normal accelerations and loads based on the controlled maintenance costs [2].

Methods for studying those accelerations or loads mainly include the theoretical, direct and indirect methods [3]. In engineering, indirect methods are the most widely used and technically mature approach. The most common indirect method is based on strain gauge load measurements, which involve calculating key loads using measured strain data and stiffness matrices [4]. Brown et al. [5] were the first to propose the vision of applying this method to the structural health monitoring system of the F-35 aircraft. Davies et al. [6] further emphasized the necessity of implementing this method for health monitoring of this aircraft model. Lei et al. [7] provided a detailed description of the method, which includes the use of load equations and strain sensor measurements to determine external loads; strain measurements are primarily employed to establish, calibrate, and optimize these load equations. Research on the use of fiber Bragg grating (FBG) sensors for strain collection has become highly advanced. Hu et al. [8] have conducted an in-depth study of these sensors, characterizing and quantifying the strain transfer mechanisms and measurement accuracy in composite structures.

However, traditional methods encounter issues with both efficiency and accuracy. First, in terms of accuracy, these conventional methods do not classify the maneuvers, and as a result, the accuracy of load analysis cannot be further improved [9]. The recognition and classification of aircraft maneuvers, also known as FMR, facilitate the establishment of distinct calculation models for training and predicting flight parameter data with different characteristics, thereby significantly enhancing accuracy [10]. Secondly, in terms of efficiency, both experimental measurements of strain and computational simulations involve high computational costs, resulting in low analytical efficiency. Currently, neural network models based on deep learning offer high research value by training on existing data to establish alternative models [11,12].

Although, one problem is that a high number of features in a dataset may lead to dimensional disaster for deep learning methods, increasing computational complexity, and leading to overfitting in some machine learning models [13]. For example, Gandy et al. [14] described the data recording system of the F-22, which captures a comprehensive set of 670 flight parameters. This dataset encompasses 219 state parameters, including normal overload, attitude angles, altitude, and velocity, alongside 451 switch parameters, such as fuel mass, landing gear status, and door positions, as depicted in Figure 1.

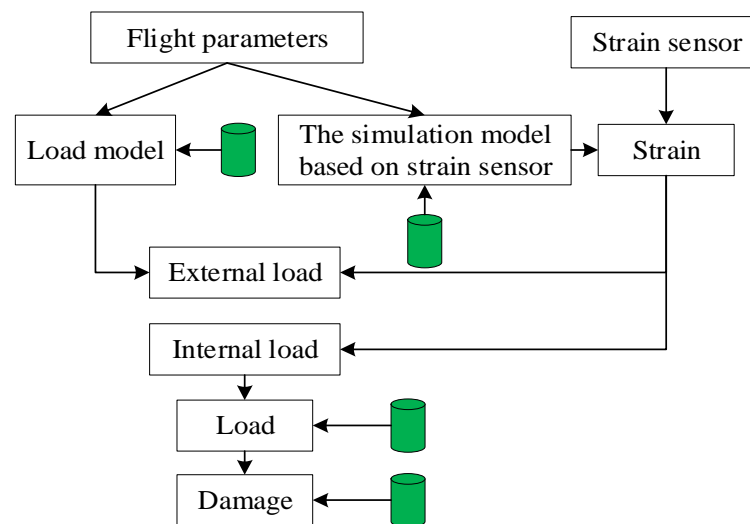


**Figure 1.** Flowchart for F-35 Aircraft load Monitoring (The green box represents the recorded data).

The higher dimensionality of the flight parameter load strains makes it more difficult to build the prediction model, Silva et al. [15] suggested that the dimensionality of the obtained flight parameters should be reduced while retaining some important dimensions. Common dimensionality reduction methods include Principal Component Analysis (PCA), AE, t-Distributed Stochastic Neighbor Embedding (t-SNE), and Locally Linear Embedding (LLE) [16], where PCA belongs to linear dimensionality reduction methods [17], while AE, t-SNE, and LLE belong to nonlinear dimensionality reduction methods [18]. Linear dimensionality reduction methods assume that data can be represented by linear transformations during the dimensionality reduction process, where the reduced features are linear combinations of the original features. PCA achieves dimensionality reduction by finding the directions of maximum variance in the data and projecting the data onto these directions [19]. Nonlinear dimensionality reduction methods, on the other hand, assume that data may contain nonlinear structures during the dimensionality reduction process, allowing for more accurate capture of complex relationships within the data structure. Among them, t-SNE is suitable for relatively small datasets, while the locality of LLE results in poor performance in preserving global structure [20]. AE are unsupervised neural network models aimed at learning data compression and are used to reconstruct the original input data [11,21]. Flight parameters are extensive, and most parameters exhibit nonlinear relationships. AE models may be more suitable for reducing the dimensions of flight data

in this case, which is an innovative approach. The neural network prediction models after AE dimensionality reduction should be selected for strain prediction of an aircraft. The recurrent neural network (RNN) [22] and LSTM [23] are the mostly used models for this purpose. However, there has been less previous research to determine which model is more suitable for predicting strain in aircraft structures.

In this paper, based on the recording data with a small fixed-wing unmanned aerial vehicle (UAV) sourced from the xx Institute of China, we identify the states of typical flight parameters, establish stiffness matrices between loads and strains through virtual ground calibration experiments, and develop a physical model to establish the mapping relationship between measured strain areas and critical strains. This provides necessary inputs and outputs to solve the mapping relationship between flight parameters and critical loads (and strains). The obtained data will serve as raw data for training AE model dimensionality reduction and deep learning neural network models, which will then be used to predict structural strains of new aircraft models and compare their accuracy. This study will proceed through five steps of strain prediction research, including dimensionality reduction of flight parameters, maneuver recognition based on flight parameters using MRF, wing virtual ground calibration testing, dimensionality reduction using AE neural networks, and strain prediction using LSTM. The research process is illustrated in Figure 2.

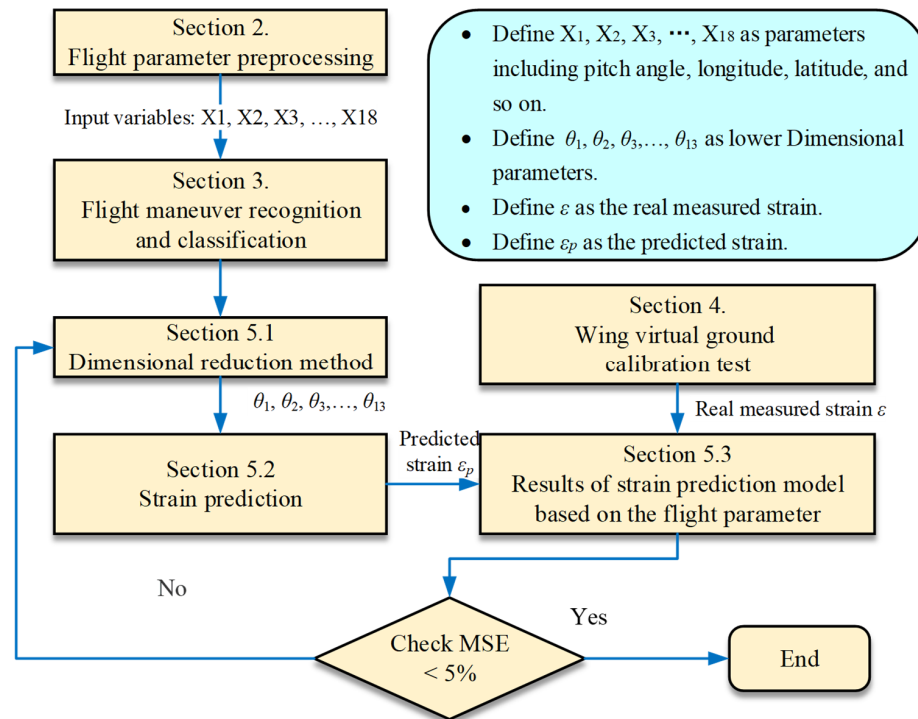


Figure 2. The flowchart of strain prediction.

## 2. Flight Parameter Preprocessing

### 2.1. Composition of the Flight Data

Flight data includes information collected by the flight recording system during the take-off and landing of the aircraft, generally including:

- (1) Flight landing and take-off labeling information, such as flight time, and flight subject, etc.;
- (2) Aircraft attitude parameters, such as altitude, speed, Mach number, latitude and longitude, wind speed, acceleration in all directions, pitch angle, and roll angle;
- (3) Information on the status of aircraft maneuver parameters, such as the deflection of the rudder and flaps as well as the position of the horizontal stabilization plane;
- (4) Condition parameters of the power unit, such as high and low-pressure engine speeds, and full engine oil level.

The main focus of this paper is to study the mapping relationship among flight parameters, strains, and loads, with an emphasis on aircraft attitude parameters and navigation position information. To meet the requirements for load identification and strain prediction, 30 common flight attitude parameters are selected for data recording and analysis, including three-axis load factors, three-axis accelerations, aircraft angle of attack, Euler angles, altitude, and speed. The selected flight attitude parameters are listed in Table 1.

**Table 1.** Flight parameters selected in the paper.

| Flight Parameter Name                           | Unit  | Flight Parameter Name                       | Unit               |
|---|-------|---|--------------------|
| Deflection Angle of Left Horizontal Stabilizer  | rad   | Pitch Angle                                 | rad                |
| Deflection Angle of Right Horizontal Stabilizer | rad   | Roll Angle                                  | rad                |
| Deflection Angle of Left Aileron                | rad   | Yaw Angle                                   | rad                |
| Deflection Angle of Right Aileron               | rad   | Axial Angular Acceleration                  | rad/s <sup>2</sup> |
| Rudder Deflection Angle                         | rad   | Normal Angular Acceleration                 | rad/s <sup>2</sup> |
| Left Leading Edge Slats Deflection Angle        | rad   | Lateral Angular Acceleration                | rad/s <sup>2</sup> |
| Right Leading-Edge Slats Deflection Angle       | rad   | Normal Load Factor                          | g                  |
| Pitch Angular Velocity                          | rad/s | Axial Load Factor                           | g                  |
| Roll Angular Velocity                           | rad/s | Lateral Load Factor                         | g                  |
| Yaw Angular Velocity                            | rad/s | Mach Number                                 | Ma                 |
| Dynamic Pressure                                | MPa   | Atmospheric Airspeed                        | m/s                |
| Total Aircraft Fuel Quantity                    | kg    | Sideslip Angle                              | rad                |
| Elevation                                       | m     | Attack Angle                                | rad                |
| Low-Pressure Turbine Speed of Right Engine      | m/s   | Low-Pressure Turbine Speed of Left Engine   | m/s                |
| High-Pressure Turbine Speed of Left Engine      | m/s   | High-Pressure Turbine Speed of Right Engine | m/s                |

## 2.2. Extraction of Effective Flight Phases

In actual flight, the flight phases include ground run, taxiing, take-off, climb, departure, aerobatics, cruise, descent, approach landing and ground taxiing. Compared to airborne flight, the ground run and taxiing phases are subjected to smaller loads. In this study, the effective flight phase is defined as the remaining flight process excluding the ground run, so that the ground taxi take-off and air maneuver cruise phases are analyzed. The judgment of the ground taxi take-off relies on the state of the landing gear, and due to the lack of landing gear information in the data, the ground speed calculated by airspeed and wind direction is used to judge the effective flight data. The correspondence between ground speed and flight phases is shown in Table 2.

**Table 2.** Correspondence between ground speed and flight phase.

| Ground Speed $v_g$ /(m/s) | Flight Stage                                 |
|---------------------------|--|
| $V_g = 0$ $v_g = 0$       | Ground run                                   |
| $v_g \leq 80$             | Taxi, take-off, approach landing, descent    |
| $v_g > 80$                | Climbing, heading out, aerobatics, cruising. |

## 2.3. Interpolated Data for Different Sampling Rate

The sampling rate refers to the frequency at which the flight reference recorder collects flight data per second. Different flight parameters have different sampling rates. For instance, parameters such as fuel load and engine RPM change slowly and do not require a high sampling rate. Moreover, increasing the sampling rate would exponentially increase the data volume. However, for subsequent training of deep learning models using sequential models, complete data are required. This poses a challenge because it leads to missing flight parameter data within the same time interval, and blindly increasing the sampling rate cannot solve this issue. To ensure data continuity, interpolation methods are typically used to fill in missing values for flight parameters with different sampling rates [24]. The filled data is presented in Table 3. The data originates from a flight of a small fixed-wing

UAV used for testing flight data, sourced from the Aircraft XX Institute of China. These data were provided to us after undergoing certain de-identification procedures.

**Table 3.** Data generated by linear interpolation method.

| Raw Data            |                                       |               | Data after Interpolation |                                       |               |
|---------------------|---------------------------------------|---------------|--------------------------|---------------------------------------|---------------|
| Total Oil Volume/kg | Low-Pressure Speed of the Left Engine | Normal Load/g | Total Oil volume/kg      | Low-Pressure Speed of the Left Engine | Normal Load/g |
| 1367                | 73.7                                  | 11.547        | 1367                     | 73.7                                  | 11.547        |
|                     |                                       | 11.406        | 1366.875                 | 73.7                                  | 11.406        |
|                     | 73.7                                  | 11.496        | 1366.75                  | 73.7                                  | 11.496        |
|                     |                                       | 11.211        | 1366.625                 | 73.65                                 | 11.211        |
|                     | 73.6                                  | 11.539        | 1366.5                   | 73.6                                  | 11.539        |
|                     |                                       | 11.070        | 1366.375                 | 73.6                                  | 11.070        |
|                     | 73.6                                  | 11.453        | 1366.25                  | 73.6                                  | 11.453        |
|                     |                                       | 11.754        | 1366.125                 | 73.6                                  | 11.754        |
| 1366                | 73.6                                  | 10.992        | 1366                     | 73.6                                  | 10.992        |

### 3. Flight Maneuver Recognition

In order to improve the identification accuracy of the load and strain models, it is necessary to identify the states of the flight parameters and build the models in the identified states, respectively. This chapter focuses on typical load state delineation and typical maneuver action delineation. The flight parameters used to delineate the states in this chapter are the flight parameters reflecting the flight attitude in the flight parameters after the removal and supplemental processing of the distorted data and the filtering process.

#### 3.1. Typical Load State Recognition

During aircraft operation, it is almost impossible to compile load spectra for all possible states due to the rapid changes in load status [25]. Therefore, this paper adopts a multi-parameter statistical combination and induction method to identify transient load states with significant impacts. After selecting 1 h takeoff and landing data, based on the classification results of typical load states, six typical load states are identified: symmetric subsonic low altitude small angle of attack (M1), symmetric subsonic low altitude large angle of attack (M2), symmetric subsonic medium altitude small angle of attack (M3), symmetric subsonic medium altitude large angle of attack (M4), symmetric subsonic high altitude small angle of attack (M5), and symmetric subsonic high altitude large angle of attack (M6). Identification is based on thresholds of several typical flight parameters, and these datasets will serve as inputs for the flight parameter neural network model in our work. Additionally, strain data measured at different positions during virtual ground calibration testing are also included as inputs. The following are the characteristic values of the selected identification results for these six load states, as shown in Table 4.

**Table 4.** Eigenvalues of the landing load state classification results of a flight.

| Rolling Angular Rate (deg/s) | Ground Speed (m/s) | Altitude (m) | Inertial Attack Angle (deg) | Strain ( $\mu\epsilon$ ) | Status Category |
|------------------------------|--------------------|--------------|-----------------------------|--------------------------|-----------------|
| 0.52                         | 199.44             | 1438         | 2.77                        | 107.69                   | M1              |
| 0.27                         | 83.44              | 1577         | 10.79                       | 388.81                   | M2              |
| −0.02                        | 211.06             | 4197         | 4.04                        | 287                      | M3              |
| −0.02                        | 201.25             | 6230         | 10.04                       | 350.97                   | M4              |
| 0.05                         | 215.25             | 7025         | 3.54                        | 501.17                   | M5              |
| −0.02                        | 193.75             | 7868         | 12.68                       | 712.12                   | M6              |

### 3.2. Flight Maneuver Recognition

Despite the preceding preprocessing, the regularity of the flight parameter data persists poorly, posing challenges in distinguishing between different maneuvers. Identifying maneuver segments is imperative, relying on the characteristics exhibited by flight parameter data of various maneuver types and comparing these traits to ascertain the corresponding maneuver segments for the current data segment. An illustration of the general maneuver recognition process is depicted in Figure 3.

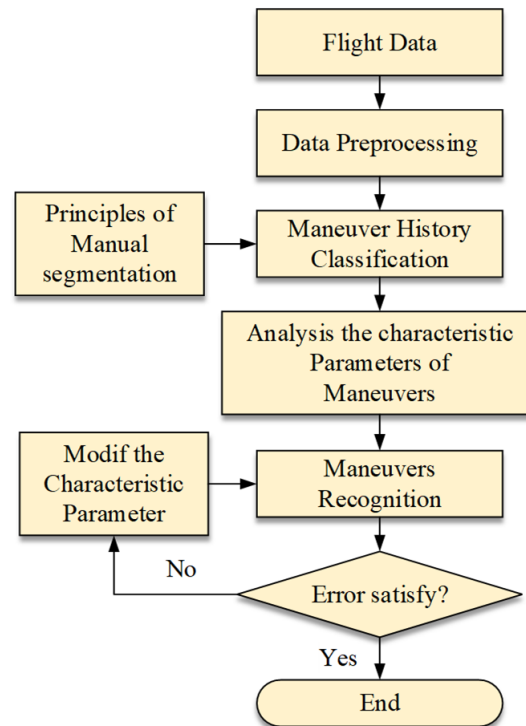


**Figure 3.** Flowchart for a general maneuver recognition method.

Generally, aircraft maneuvers are classified into three categories: vertical plane, horizontal plane, and spatial maneuvers. The maneuver recognition algorithm based on the time series of significant points, utilizing the trend states of trajectories projected onto the horizontal and vertical planes, which can be referred to our previous proposed Sequence Important Point-Based Method. The specific steps are as follows:

Step 1: Divide the flight parameters into multiple segment sequences with fixed lengths, and then project the trajectory of each sequence onto the horizontal plane.

Step 2: Apply certain merging rules, utilizing the piecewise linear representation and perceptually important point algorithm (PLR-PIP) to segment the trajectory projection, identify the sequence trend, and merge adjacent trend sequences with the same state.

Step 3: Project the merged trend sequences onto the vertical plane; then, the PLR-PIP algorithm is used to segment the trajectory projection, identify the sequence trend, and subdivide the trend sequences by subdivision rules.

Step 4: Superimpose the trend states of the two plane projections to obtain the basic aircraft maneuvers, as illustrated in Figure 4.

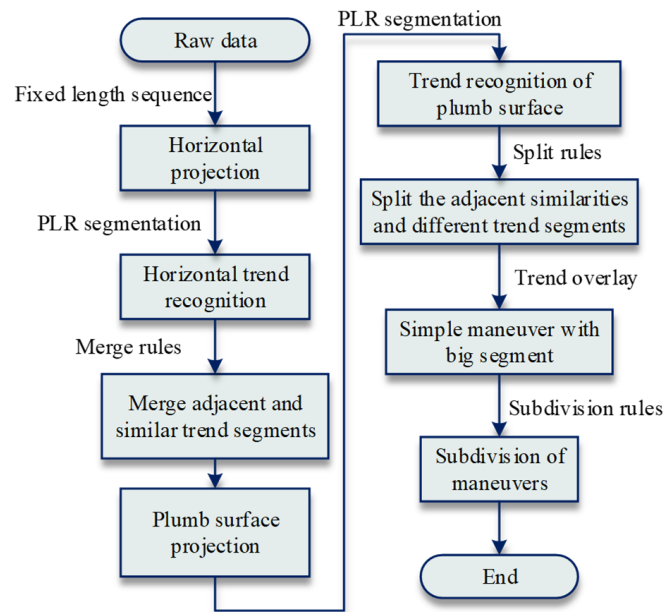


**Figure 4.** The flow chart of proposed sequence important point-based method.

Details can be found in our previous work [26].

#### 4. Strain Measurement and Calculation of Wings

Finite element modeling (FEM) and virtual strain gauges for ground calibration testing were utilized. This process allowed us to establish stiffness matrices and correlation matrices between load input and strain gauge output paths, enabling us to obtain strain data for the aircraft wing.

##### 4.1. Finite Element Modelling

The 3D shell cells of the wing model were discretized using Finite Element Analysis (FEA) software HyperMesh (Ansys 19.0) [7]. Unnecessary edges and lines were removed, and the model was geometrically processed into a common nodal model. The mesh used in this study consisted of S4R elements, which are four-node surface thin shell elements aimed at reducing integration and eliminating circular controls. The mesh size was 10, resulting in a total of 83,990 elements. The wing material chosen was LY12, and based on ground calibration tests, the wing components were firmly connected to the fuselage structure. The boundary conditions for virtual ground calibration testing were applied at the nodes where the wing connects to the fuselage in the finite element model. These boundary conditions were restricted to six degrees of freedom. The boundary conditions for virtual ground calibration testing were applied to all nodes connected to the wing and fuselage junction, and constrained to have six degrees of freedom, representing a fully fixed support.

The FEM of the wing is depicted in Figure 5.

(a) Schematic diagram of the wing finite element method (FEM): This diagram illustrates the structural analysis of the wing using the finite element method, which is a computational tool for predicting the behavior of the wing under various loading conditions. The engine loads were not directly simulated, because the engine layout of this type of Unmanned Aerial Vehicle (UAV) is within the fuselage. However, the loads were correlated with strains by extracting corresponding loads from the FE model provided by the research institute.

(b) Arrangement of the Bending Moment Bridge: Based on the structural characteristics of the wing, the upper and lower flanges of the wing beam primarily bore the bending moments generated by the wing. Consequently, the bending moment strain gauge bridges were positioned on the upper and lower flanges of the wing beam at the section where measurements are taken. Strain gauge bridges numbered 1 and 4 were placed along the

lengthwise direction of the flanges, while strain gauge bridges numbered 2 and 3 were oriented perpendicular to bridges 1 and 4, respectively.

(c) Arrangement of the Shear Bridge: The webs and skins of the wing beam and rib primarily withstand the shear forces produced by the wing. Therefore, the shear strain gauge bridges were positioned on the neutral axis or a location close to the neutral axis of the webs and skins of the wing beam and rib. A shear full bridge, composed of four strain gauges arranged at 90-degree intervals to each other, was used to measure the shear forces. This arrangement ensures that the relative bending moment load was minimized, and it was the direction where the maximum shear stress could be most accurately measured by the strain gauges.

(d) Arrangement of the torque bridge: The wing box of the aircraft wing is mainly subjected to the torque generated by the wing. Hence, the torque strain gauge bridges were positioned at the center of the skin of the wing box section where measurements were conducted. A torque full bridge, consisting of four strain gauges arranged at 90-degree intervals, was utilized to measure the torque. This configuration allowed for the accurate detection of the torque effects on the wing structure.

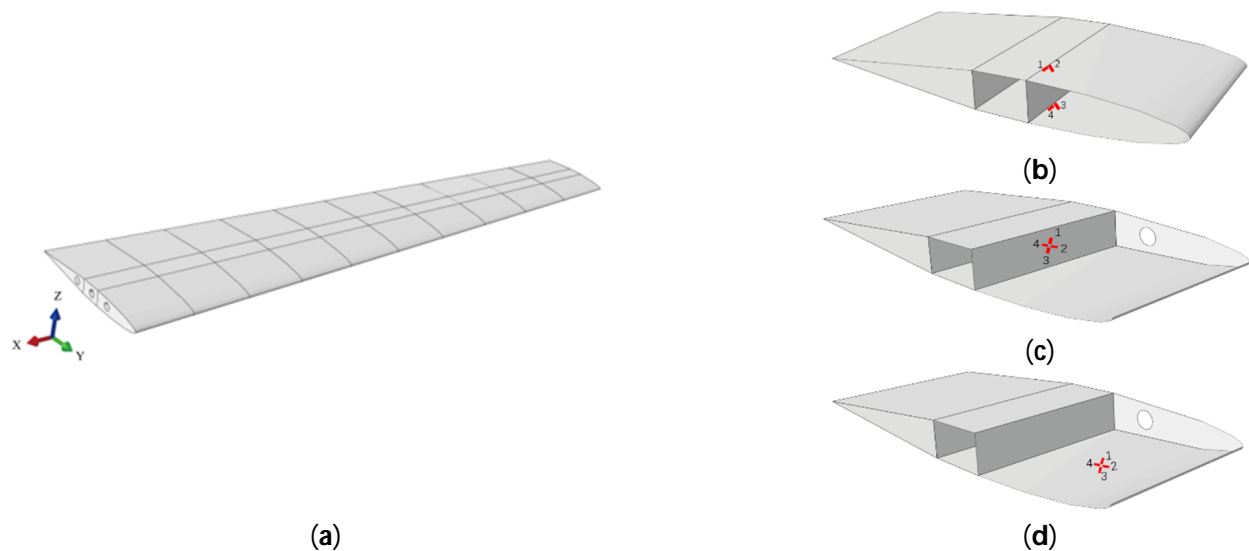


**Figure 5.** Schematic wing diagram of the FEM and bridge arrangements: (a) schematic diagram of the wing FEM; (b) arrangement of bending moment bridge; (c) arrangement of the shear bridge; and (d) arrangement of the torque bridge.

#### 4.2. Virtual Strain Bridge

Owing to the complexity of the wing structure and loading conditions, strain often arises from the combination of multiple loads. To decouple this strain data, the design of the placement and paths of strain gauge components must allow for the separation of multiple loads. The Virtual Strain Bridge technique is an advanced method employed for measuring material strain, renowned for its non-contact nature, high accuracy, and flexible arrangement. This paper employed this method for strain measurement.

##### 4.2.1. Arrangements of Virtual Strain Bridges

The arrangement of strain bridges should ensure accurate and reliable measurement of the structure's strain. This requires selecting appropriate placement positions and orientations.

The upper and lower spar caps of the wing beam primarily withstand the bending moment generated by the characteristics of wing's structural force. Bending moment strain gauges No. 1 and No. 4 were positioned along the length of the spar caps, while strain gauges No. 2 and No. 3 were oriented perpendicular to strain gauges No. 1 and No. 4. The ribs and web of the wing beam, along with the wing skin, primarily experienced shear forces generated by the wing. Each shear strain gauge comprised four interconnected 90°

strain gauges. The arrangement of shear strain gauges is illustrated in Figure 5c. The wing box primarily experienced torsional forces generated by the wing. Each torsion strain gauge comprised four interconnected 90° strain gauges. The arrangement of torsion strain gauges is illustrated in Figure 5d.

#### 4.2.2. The formation of Virtual Strain Bridge

The ground calibration test strain group bridge method utilized a Wheatstone full bridge, comprising four strain gauges employing the group bridge method depicted in Figure 6. Each strain bridge represented a bridge arm, providing strain data based on the layout position and direction.

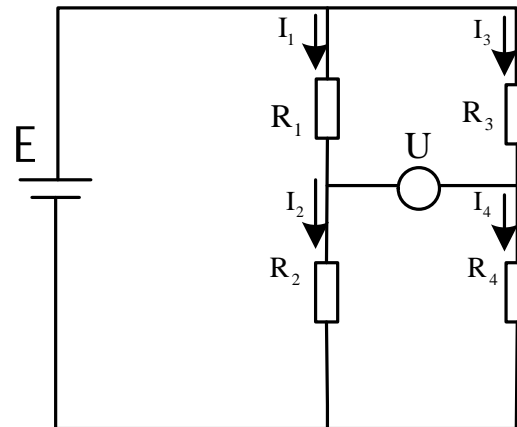


Figure 6. Diagram of bridge group method.

#### 4.2.3. Strain Measurement by Virtual Strain Bridge

The strain response of the four virtual strain bridges arranged at the top and bottom rim strips of the wing girder was denoted as  $\varepsilon_1$ ,  $\varepsilon_2$ ,  $\varepsilon_3$ ,  $\varepsilon_4$ , while the response of the bending moment virtual bridge was represented as

$$X_{bm} = \varepsilon_1 + \varepsilon_3 - \varepsilon_2 - \varepsilon_4 \quad (1)$$

where  $\varepsilon_1$  and  $\varepsilon_4$  could be directly extracted from the nodal strains of the finite element results,  $\varepsilon_1$  and  $\varepsilon_2$  were obtained from the equations of mechanics of materials:

$$\varepsilon_2 = -\mu\varepsilon_1, \varepsilon_3 = -\mu\varepsilon_4 \quad (2)$$

where  $\mu$  represents the Poisson's ratio of the material at the location where the strain bridge is affixed. Then, the strain response of the bending moment bridge is

$$X_{bm} = (1 + \mu)(\varepsilon_1 - \varepsilon_4) \quad (3)$$

The calculation of shear force and torque can be referred by the virtual strain bridge, which is in Appendix A.1 Note 1.

#### 4.3. Definition of Load Condition

The load of the ground calibration test includes three factors: loading point, loading direction and load value. Usually, in the FEM, the intersection point of the wing beam and the wing rib is selected as the loading point, including single point and multi-point; the loading direction is generally perpendicular to the wing surface, upwards or downwards; the load is loaded step by step under different working conditions, and the load condition of each working condition is satisfied by transforming the position of the loading point. The magnitude of the load (5 kN) primarily originates from the surface pressure of the wings and the equivalent engine load on the fuselage, which are obtained through strain

gauges and sensors attached to critical components. In this article, the magnitude of loads was directly extracted from the FE model provided by the research institute. The boundary conditions were defined as shown in Figure 7a, and the calibration load was applied vertically upwards at the intersection of the wing rib and the wing beam; the loading point is shown in Figure 7b.

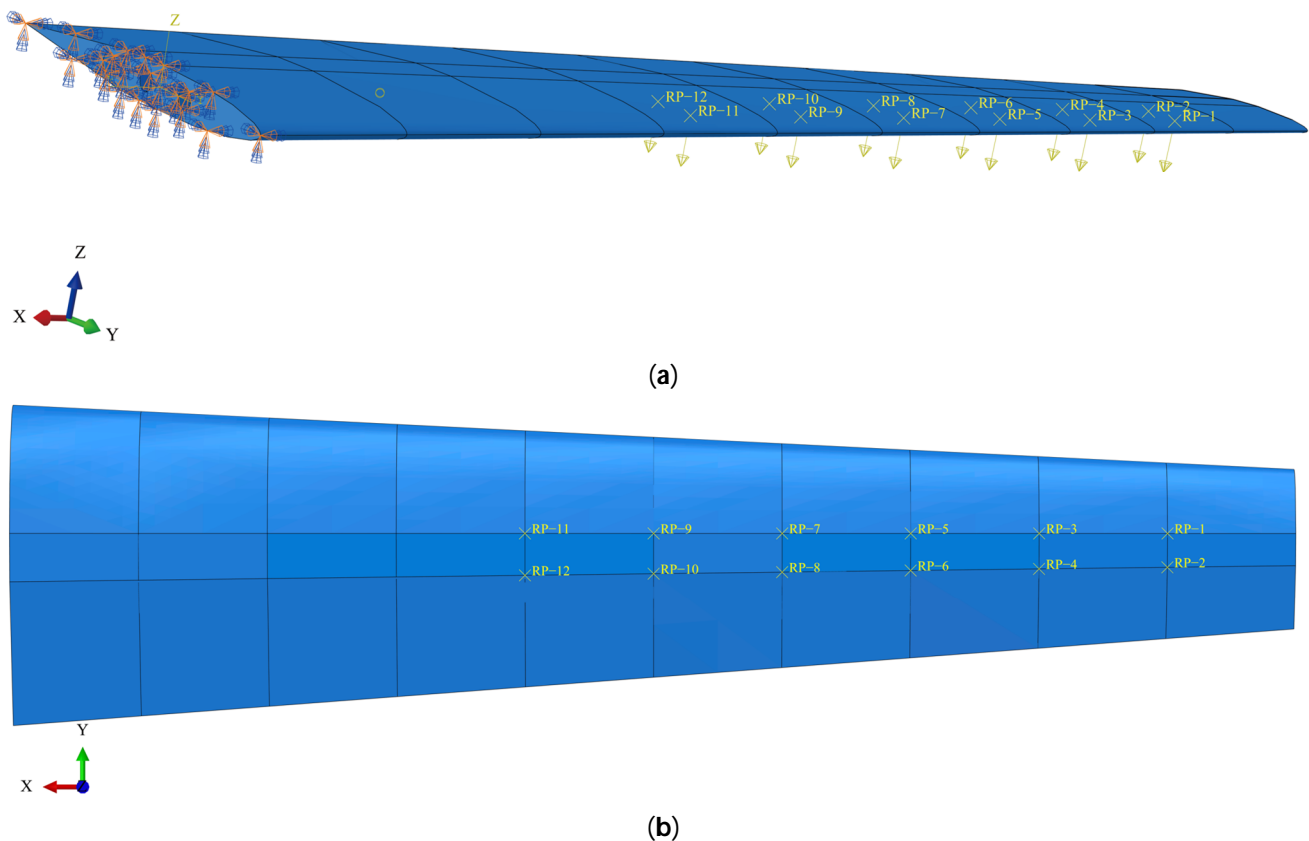


**Figure 7.** Virtual ground calibration test. (a) Boundary conditions; (b) positions of the loading points.

#### 4.4. Virtual Calibration Sample Data

##### 4.4.1. Load Strain Sample Data

After completing the virtual ground calibration experiment, it is imperative to analyze the response of the strain gauges to ascertain their suitability for integration into the load equation. Details can be found in Appendix A.2 Note 2. After considering the repeatability of strain gauge responses and loading conditions, the loads were applied at the intersection points near the wingtip of the wing beams and ribs. Subsequently, calibration equations for the load-strain data at six single-point loads, namely RP1, RP3, RP5, RP7, RP9, and RP11, were derived. The data for each loading point included the shear force, bending moment, torsional moment, the response values of bending moment, torsional moment and shear strain gauges measuring the load profiles. The original data of the loading model are presented in Table 5, which will serve as the training sample library for subsequent deep learning models.

As shown in Table 5, there was a significant disparity between the values of loads and strain data. In order to improve the identification accuracy of the load model, the data were normalized prior to modeling [27]. Additionally, the actual load data can be obtained through inverse normalization [28]. The normalized load and strain data are presented in Table 6.

**Table 5.** Load modelling raw data.

| Shear Force (kN) | Bending Moment (kN·m) | Torque (kN·m) | The Bending Moment Bridge ( $\mu\epsilon$ ) | Shear Bridge ( $\mu\epsilon$ ) | Torque Bridge ( $\mu\epsilon$ ) |
|------------------|-----------------------|---------------|---|--------------------------------|---------------------------------|
| 5                | 14.91                 | 1.66          | 2014.02                                     | −184.3                         | 63.2                            |
| 8                | 20.67                 | 2.38          | 2788.74                                     | −319.26                        | 73.72                           |
| 10               | 21.85                 | 2.62          | 2947.55                                     | −427.91                        | 54.27                           |
| 15               | 26.8                  | 3.41          | 3606.49                                     | −687.65                        | 24.54                           |
| 18               | 24.99                 | 3.47          | 3357.53                                     | −874.91                        | −39.75                          |
| 20               | 19.8                  | 3.16          | 2655.46                                     | −1030.43                       | −113.17                         |

**Table 6.** Normalized load strain data.

| Shear Force (kN) | Bending Moment (kN·m) | Torque (kN·m) | The Bending Moment Bridge ( $\mu\epsilon$ ) | Shear Bridge ( $\mu\epsilon$ ) | Torque Bridge ( $\mu\epsilon$ ) |
|------------------|-----------------------|---------------|---|--------------------------------|---------------------------------|
| −1.0000          | −1.0000               | −1.0000       | −1.0000                                     | 1.0000                         | 0.8874                          |
| −0.6000          | −0.0314               | −0.2063       | −0.0270                                     | 0.6810                         | 1.0000                          |
| −0.3333          | 0.1675                | 0.0658        | 0.1724                                      | 0.4242                         | 0.7919                          |
| 0.3333           | 1.0000                | 0.9388        | 1.0000                                      | −0.1898                        | 0.4737                          |
| 0.7333           | 0.6953                | 1.0000        | 0.6873                                      | −0.6324                        | −0.2143                         |
| 1.0000           | −0.1779               | 0.6552        | −0.1944                                     | −1.0000                        | −1.0000                         |

#### 4.4.2. Strain Sample Data at Critical Locations

Since the processing method is unchanged, the strain data for the critical parts are given here, the raw strain data are shown in Table 7 and the normalized strain data are shown in Table 8.

**Table 7.** Raw strain data for critical sites.

| Loads | Strain of Critical Position ( $\mu\epsilon$ ) | The Bending Moment Bridge ( $\mu\epsilon$ ) | Shear Bridge ( $\mu\epsilon$ ) | Torque Bridge ( $\mu\epsilon$ ) |
|-------|---|---|--------------------------------|---------------------------------|
| 5     | 2093.2  | 2014.02                                     | −184.3                         | 63.2                            |
| 8     | 2957.07                                       | 2788.74                                     | −319.26                        | 73.72                           |
| 10    | 3206.18                                       | 2947.55                                     | −427.91                        | 54.27                           |
| 15    | 4076.41                                       | 3606.49                                     | −687.65                        | 24.54                           |
| 18    | 4005.85                                       | 3357.53                                     | −874.91                        | −39.75                          |
| 20    | 3466.17                                       | 2655.46                                     | −1030.43                       | −113.17                         |

**Table 8.** Normalized strain data for key structures.

| Loads | Strain of Critical Position ( $\mu\epsilon$ ) | The Bending Moment Bridge ( $\mu\epsilon$ ) | Shear Bridge ( $\mu\epsilon$ ) | Torque Bridge ( $\mu\epsilon$ ) |
|-------|---|---|--------------------------------|---------------------------------|
| 5     | −1  | −1  | 1                              | 0.88742                         |
| 8     | −0.1288                                       | −0.02702                                    | 0.68099                        | 1                               |
| 10    | 0.1224  | 0.17243                                     | 0.42418                        | 0.79186                         |
| 15    | 1   | 1   | −0.18977                       | 0.4737                          |
| 18    | 0.9288  | 0.68733                                     | −0.6324                        | −0.2143                         |
| 20    | 0.3846  | −0.19441                                    | −1                             | −1                              |

## 5. Strain/Load Prediction Based on Deep Learning Model

The input data were obtained through the previous sections, which included preprocessing, flight parameter maneuver recognition classification, and wing virtual ground calibration tests. The deep learning model incorporated the AE, RNN, and LSTM models, considering the time-sequential characteristics of the flight parameters and strains/loads.

### 5.1. Dimensionality Reduction by Neural Networks

An AE network model consists of two parts, the encoder and the decoder networks, as shown in Figure 8. The encoder maps the input data to the latent space (or low dimensional space), while the decoder maps the latent data back to the original dimensional data space. Typically, the encoder contains one or more hidden layers with a decreasing number of nodes that ultimately generate the latent representation. The structure of a decoder is usually the opposite of an encoder, containing one or more hidden layers with a progressively increasing number of nodes. The objective of an AE model optimization is to minimize the reconstruction error between the input data and the reconstruction data. The most common objective function is Mean Squared Error (MSE), which minimizes the reconstruction error by adjusting the weights of the encoder and decoder.

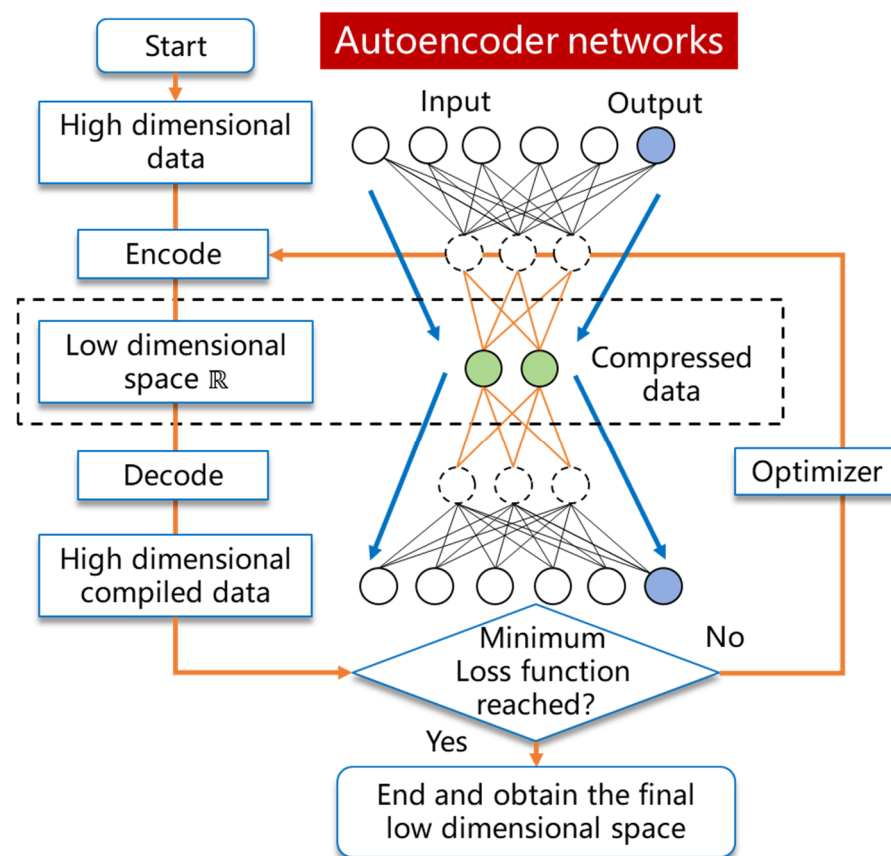


Figure 8. The structure of AE model.

The settings of some methods can be found in SI Note 3, respectively. Using 18 flight parameters such as altitude, Mach number, center of gravity normal overload, attack angle, aileron deflection, roll angular velocity, and others as inputs to the neural network model for dimensionality reduction, the target dimensionality after reduction was set to 13. Figure 9a displays the visualization results obtained by transforming the data reduced by AE using local linear interpolation method into a new three-dimensional space. Clustering was also performed, with colors representing the classes to which each data point belongs; different colors indicate different clusters. Figure 9b illustrates the Mean Squared Error (MSE) data of the reconstructed data  $\hat{X}_i$  by the encoder, denoted as

$$MSE = \frac{1}{n} \sum_{i=1}^n (X_i - \hat{X}_i)^2$$

which represents the numerical value of information loss during the encoding and decoding process. Notably, the maximum MSE does not exceed 0.068, meeting the requirements.

From these dimensionality reduction graphs, it is evident that the AE exhibits the most accuracy and stability among all dimensions based on Figure 9c.

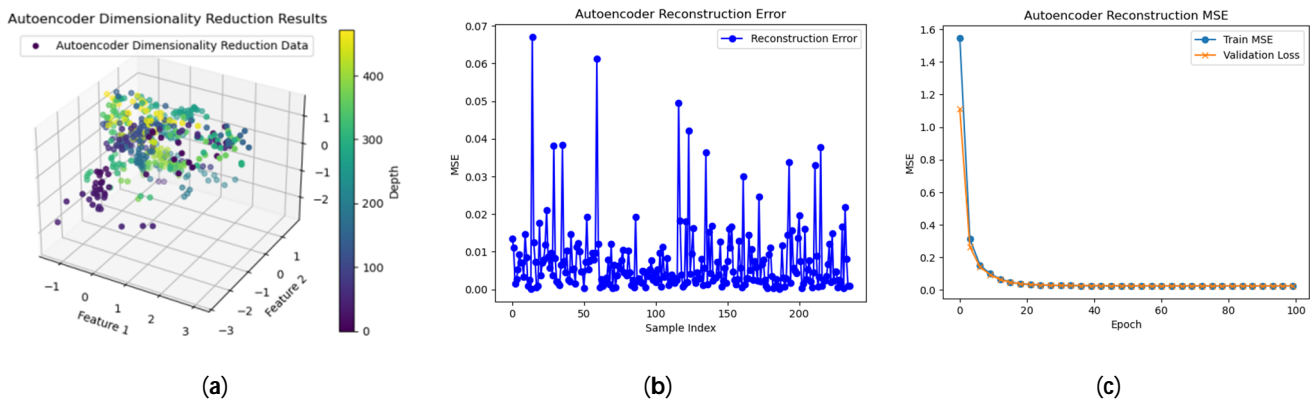


**Figure 9.** The results of dimensionality reduction achieved by AE model: (a) results of dimensional clusters; (b) the mean squared error (MSE) of reconstruction; (c) the change history of MSE along with time sequence.

The reconstruction MSEs of the LLE and PCA models, both of which are higher than that of the AE model, are shown in Figures 10a and 10b, respectively, under the same parameter settings (detailed settings can be found in Appendix A.3 Note 3). This demonstrates that the AE model achieves the highest accuracy in reconstructing the lower-dimensional parameters back to their original dimensional space.

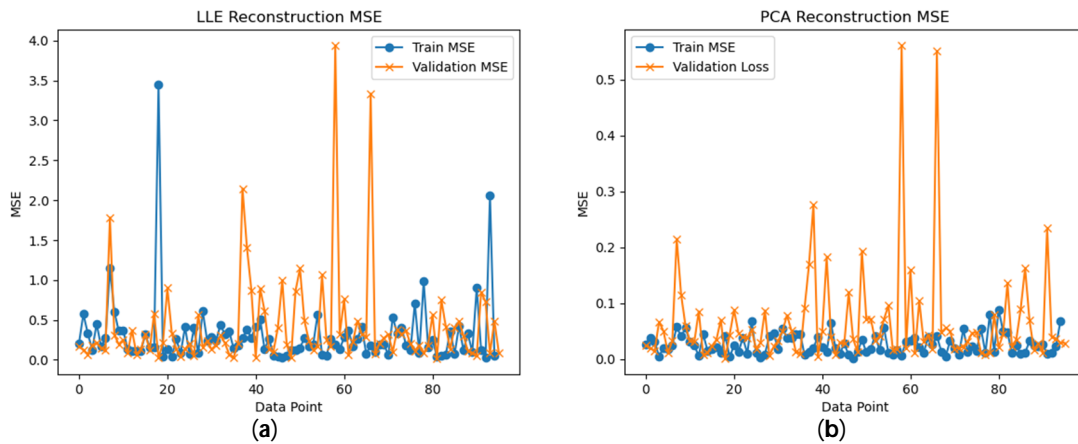


**Figure 10.** The mean squared error (MSE) of reconstruction by (a) LLE model and (b) PCA model.

### 5.2. Deep Learning Modelling for Strain Prediction

A neural network prediction model is also required after downscaling the high-dimensional data using an AE. Figure 11 illustrates the MSE error plots of the RNN and LSTM prediction models based on part of our processed data, respectively. With an increase in the number of iterations, the dataset errors of both network models can converge to 0. Specifically, the dataset errors of the RNN model converge at epochs = 43, while those of the LSTM model converge at epochs = 30, indicating a significantly faster convergence speed for the LSTM model compared to the RNN model. Therefore, the LSTM network can ensure both the convergence speed and the training accuracy of the flight parameter–strain model, which was selected as the deep learning prediction model.

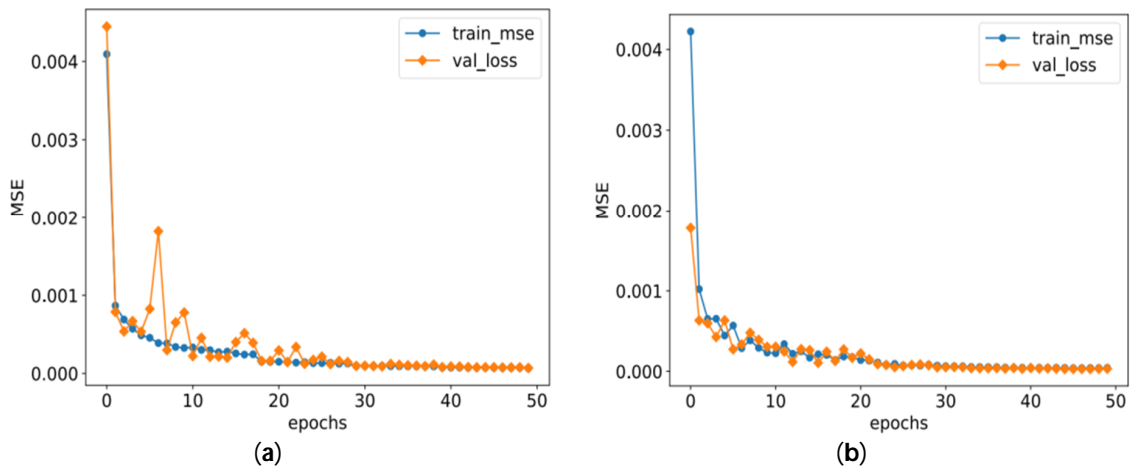


Figure 11. MSE plot obtained by (a) RNN deep learning model and (b) LSTM deep learning model.

5.3. Flight Parameter–Strain Model Simulation Results

Although it has been validated in the previous step that the LSTM deep learning model may offer better accuracy, both LSTM and RNN were still employed to train on all input data. Using AE, the 18 flight parameters (such as pitch angle, pitch rate, roll rate, yaw, angular velocity, longitudinal acceleration, lateral acceleration, normal acceleration, roll angle, ground speed, heading angle, altitude, inertia, etc.) were reduced (dimensionality reduction) to 13, and then RNN and LSTM prediction models were used separately to predict strain data. Figure 12a,b show the comparison results between real flight data and the predicted one by (a) LSTM model and (b) RNN model predicted data and real data. Generally, large strains are predominant in structural damage, so it is important that the predicted values should ideally cover the true values of large strain amplitudes as much as possible. Evidently, in Figure 12b, the RNN model significantly underestimated a large portion of the true strain values indicated by blue, potentially placing the structural design strength of the aircraft in an unsafe condition or uncontrolled risk.

Figure 13 displays the results of LSTM with FMR and without FMR at different maneuvers (State 1 and 3). Observably, after FMR processing, the prediction accuracy of the data significantly improves, particularly in predicting the maximum amplitude of strain. Furthermore, the area of the 95% confidence interval decreases substantially, indicating a reduction in uncertainty. This highlights the indispensability of FMR as a preprocessing step in the deep learning strain prediction model based on a considerable amount of flight parameter data.

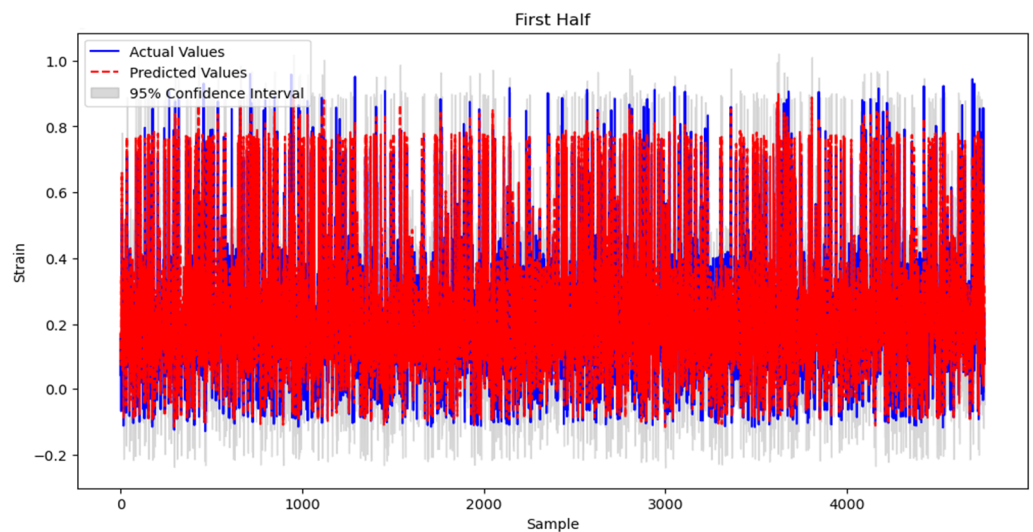
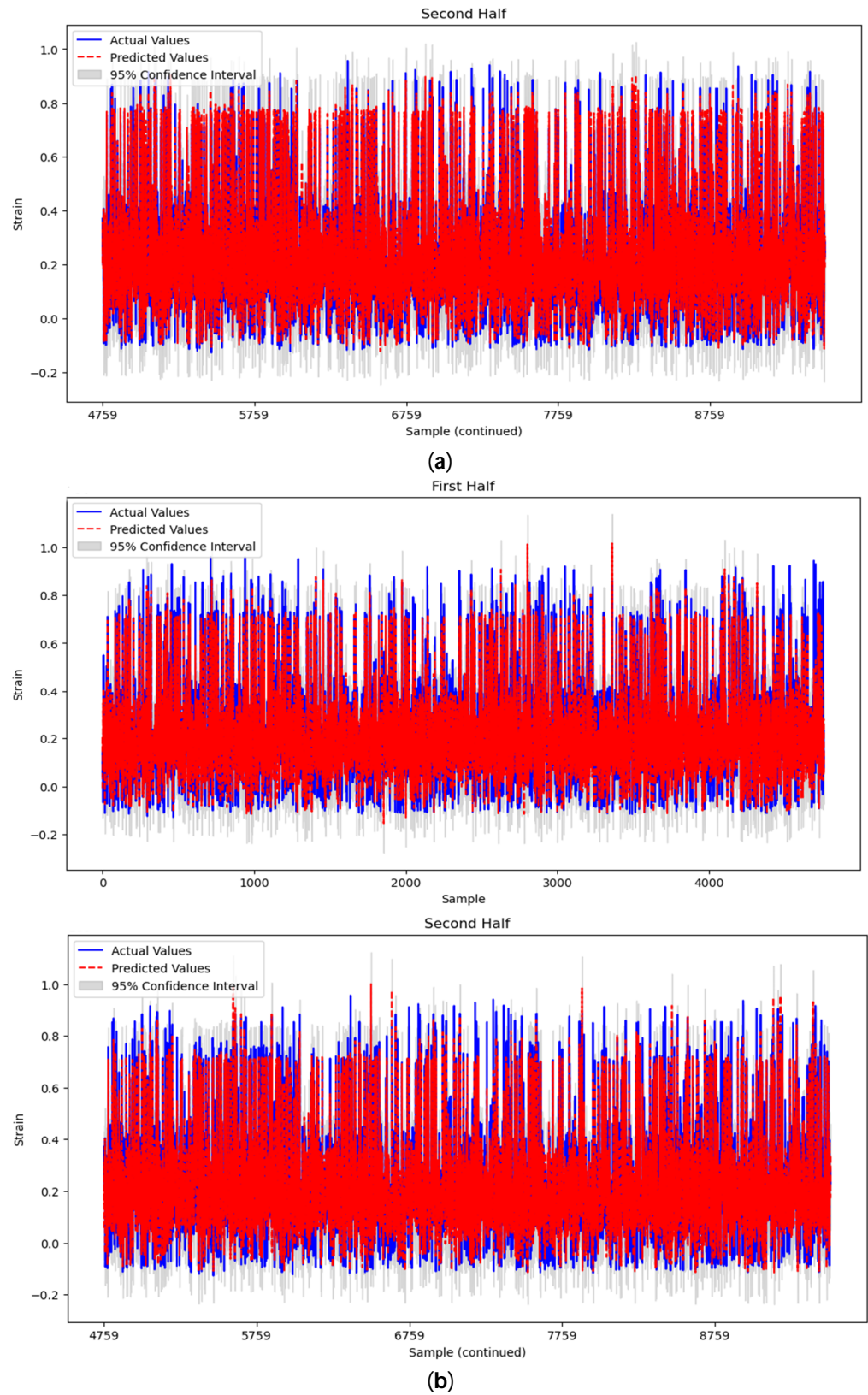
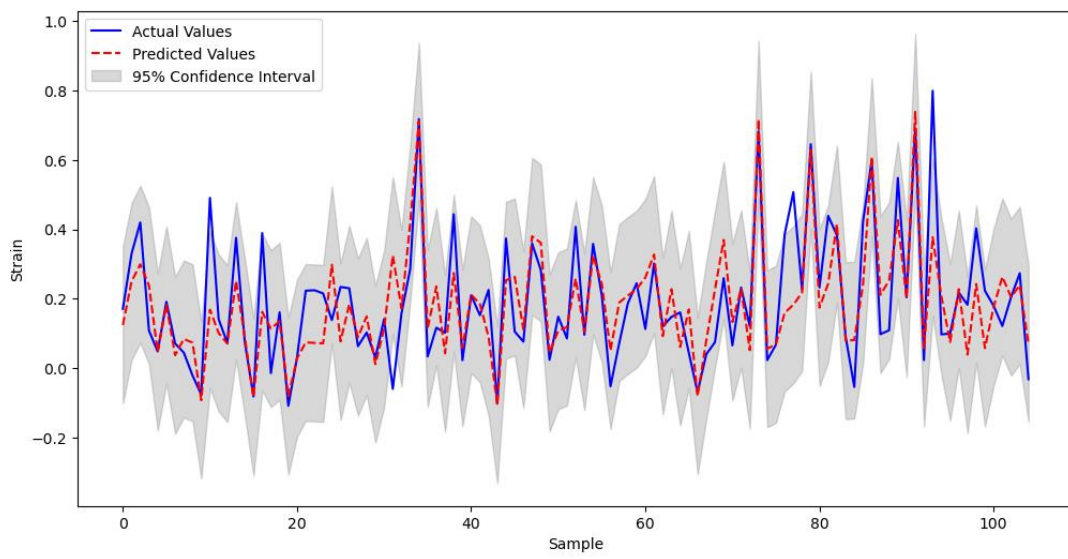


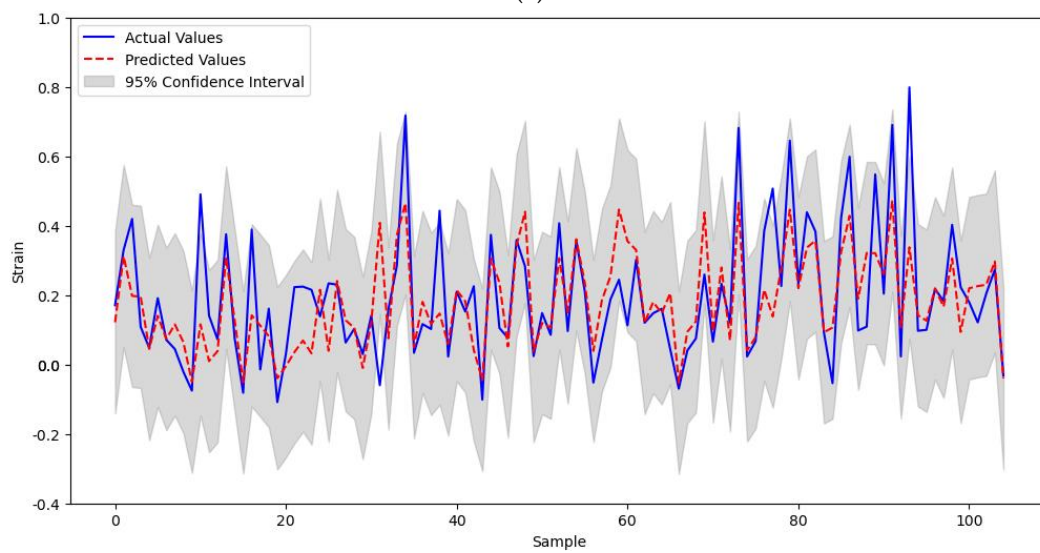
Figure 12. Cont.



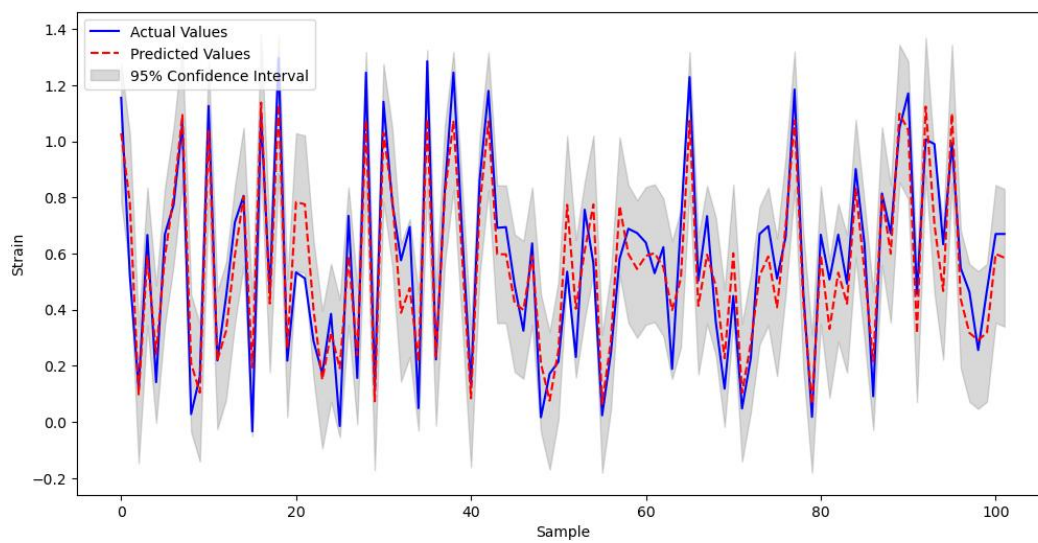
**Figure 12.** Comparison results between real flight data and the predicted one by (a) LSTM model and (b) RNN model predicted data and real data.



(a)



(b)



(c)

Figure 13. Cont.

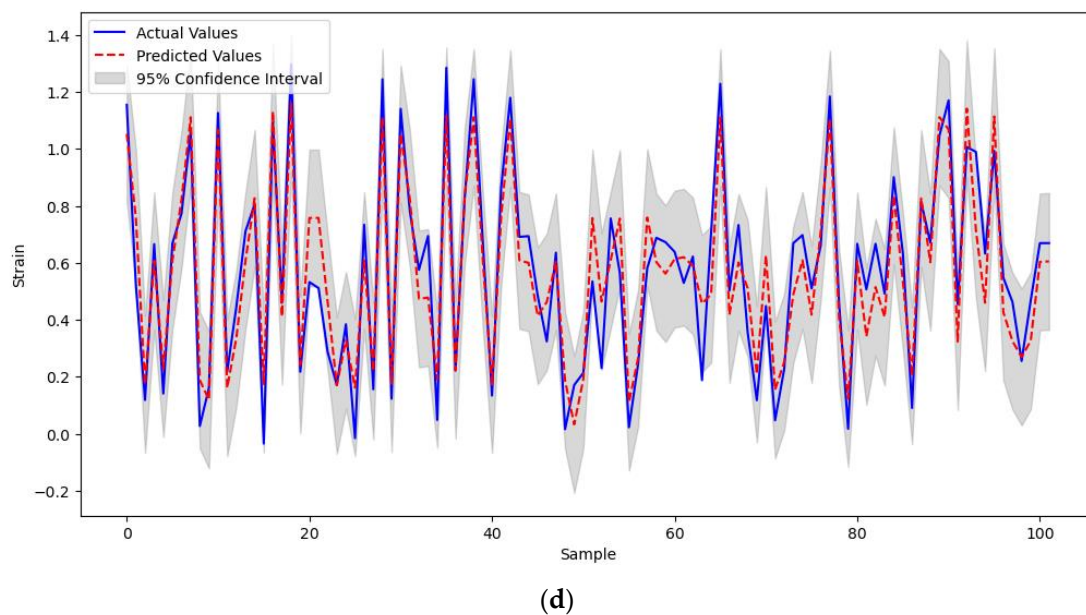


**Figure 13.** Comparison results by LSTM: (a) with FMR at maneuver state 1; (b) without FMR at maneuver state 1; (c) with FMR at maneuver state 3; (d) without FMR at maneuver state 3.

## 6. Conclusions

This study focuses on the flight parameters obtained from a certain type of aircraft, combined with data processing methods (pre-processing interpolation, flight maneuver recognition), and wing virtual ground calibration experiments. The study obtained complete flight data including strain based on this, and established a high-precision flight parameter-strain prediction model. Considering the large volume and high dimensionality of the flight data, the study (1) adopted flight maneuver recognition (FMR) to segment aircraft maneuver actions, segmenting different maneuver actions for targeted deep learning training, thus improving prediction accuracy; (2) Autoencoder (AE) neural network models were used for data dimensionality reduction, reducing the dimensions of subsequent learning models to improve accuracy while increasing efficiency. The study draws several conclusions as follows:

- (1) Compared to methods such as locally linear embedding (LLE), principal component analysis (PCA), etc., the AE model has the smallest maximum MSE (the maximum MSE does not exceed 0.068, meeting the requirements), and the clustering effect is also obvious. Under equal conditions, the priority should be given to the AE model for flight data dimensionality reduction.
- (2) The long short-term memory (LSTM) model has temporal characteristics. Combined with the AE model and FMR, this model can accurately estimate the load or strain of key parts. Particularly, the accuracy of predicting strain amplitudes is higher than that of RNN and other neural network models.
- (3) Compared to recurrent neural network (RNN) model, the LSTM model has a smaller area of uncertainty within the 95% confidence interval, indicating better stability. Therefore, the LSTM model is more suitable for learning and training the flight data model, and can be also used for subsequent preparation of the aircraft load and stress spectrum.

In conclusion, future research can utilize specific flight data for a particular aircraft type as the main dataset. Based on the methods proposed in this paper, including flight data preprocessing, FMR, and data obtained from virtual ground calibration tests, combined with the AE dimensionality reduction and LSTM method, a flight parameter-strain prediction model can be established to analyze aircraft loading and damage conditions.

**Author Contributions:** Conceptualization, W.H.; Methodology, W.H. and R.W.; Software, R.W.; Validation, W.H. and R.W.; Formal analysis, W.H.; Investigation, R.W.; Resources, W.H.; Data curation, W.H.; Writing—original draft preparation, W.H. and R.W.; Writing—review and editing, W.H. and M.Z.; Supervision, W.H. and Z.Y.; Project administration, M.Z. and Z.Y.; Funding acquisition, M.Z. and Z.Y. All authors have read and agreed to the published version of the manuscript.

**Funding:** This work was supported by the National Natural Science Foundation of China (Grant Nos. 12302156 and 52305273), China Postdoctoral Science Foundation (Grant No. 2023M742572), Natural Science Basic Research Program of Shaanxi (Program No. 2023-JC-QN-0012), Guangdong Basic and Applied Basic Research Foundation (Grant 2022A1515110636).

**Institutional Review Board Statement:** Not applicable.

**Informed Consent Statement:** Not applicable.

**Data Availability Statement:** The original contributions presented in the study are included in the article, further inquiries can be directed to the corresponding authors.

**Conflicts of Interest:** The authors declare that the research was conducted in the absence of any commercial or financial relationships that could be construed as a potential conflict of interest.

## Appendix A

### Appendix A.1. Note 1 Shear Stress and Torque Virtual Strain

The strain response of the four virtual strain bridges arranged in the webs of the wing girder is  $\varepsilon_1, \varepsilon_2, \varepsilon_3, \varepsilon_4$ , then the response of the shear force virtual bridge is

$$X_{sf} = \varepsilon_1 + \varepsilon_3 - \varepsilon_2 - \varepsilon_4 \tag{A1}$$

Nodal strains  $\varepsilon_1, \varepsilon_2, \varepsilon_3, \varepsilon_4$  cannot be extracted directly from the finite element results. Using the knowledge about plane problem in finite element [29], the nodal strains extracted from finite elements are used to calculate  $\varepsilon_1, \varepsilon_2, \varepsilon_3, \varepsilon_4$ . The theory and solution method for building a strain bridge are described below.

The shell cell of the simplified wing model belongs to the planar problem, the strain vector can be expressed as:

$$\begin{Bmatrix} \varepsilon_x \\ \varepsilon_y \\ \varepsilon_{xy} \end{Bmatrix} = \begin{bmatrix} \frac{\partial}{\partial x} & 0 \\ 0 & \frac{\partial}{\partial y} \\ \frac{\partial}{\partial y} & \frac{\partial}{\partial x} \end{bmatrix} \begin{Bmatrix} u \\ v \end{Bmatrix} = [L][N]\{\delta\}^e = [B]\{\delta\}^e \tag{A2}$$

The strain matrix  $[B]$  in Equation (A3) is expressed in terms of nodal chunks as  $[B] = [B_1, B_2, B_3, B_4]$ , Where:

$$[B_i] = \begin{bmatrix} \frac{\partial N_i}{\partial x} & 0 \\ 0 & \frac{\partial N_i}{\partial y} \\ \frac{\partial N_i}{\partial y} & \frac{\partial N_i}{\partial x} \end{bmatrix} (i = 1, 2, 3, 4) \tag{A3}$$

For a general-shaped planar domain, it can be subdivided into arbitrary quadrilaterals, in which a local coordinate system is constructed, ensuring specific numerical values at the boundary points. All points within this domain correspond to points in the established local coordinate system, enabling the mapping of the actual element to a square.

Therefore:

$$\begin{Bmatrix} \frac{\partial N_i}{\partial \xi} \\ \frac{\partial N_i}{\partial \eta} \end{Bmatrix} = \begin{bmatrix} \frac{\partial x}{\partial \xi} & \frac{\partial y}{\partial \xi} \\ \frac{\partial x}{\partial \eta} & \frac{\partial y}{\partial \eta} \end{bmatrix} \begin{Bmatrix} \frac{\partial N_i}{\partial x} \\ \frac{\partial N_i}{\partial y} \end{Bmatrix} = [J] \begin{Bmatrix} \frac{\partial N_i}{\partial x} \\ \frac{\partial N_i}{\partial y} \end{Bmatrix} \tag{A4}$$

From Equation (A4), we get.

$$\begin{bmatrix} \frac{\partial N_i}{\partial x} \\ \frac{\partial N_i}{\partial y} \end{bmatrix} = [J]^{-1} \begin{Bmatrix} \frac{\partial N_i}{\partial \xi} \\ \frac{\partial N_i}{\partial \eta} \end{Bmatrix} \tag{A5}$$

where:

$$[J] = \begin{bmatrix} \frac{\partial x}{\partial \xi} & \frac{\partial y}{\partial \xi} \\ \frac{\partial x}{\partial \eta} & \frac{\partial y}{\partial \eta} \end{bmatrix} = \frac{1}{4} \begin{bmatrix} -(1-\eta) & 1-\eta & 1+\eta & -(1+\eta) \\ -(1-\xi) & -(1+\xi) & 1+\xi & 1-\xi \end{bmatrix} \begin{bmatrix} x_1 & y_1 \\ x_2 & y_2 \\ x_3 & y_3 \\ x_4 & y_4 \end{bmatrix} \tag{A6}$$

In the formula,  $x_i, y_i$  is the value of the node coordinates, and replacing Equation (A5) into Equation (A6) to obtain the strain matrix  $[B]$ , so that the strain at any point on the plane can be obtained. At this point, the response of the virtual strain bridge can be solved from the nodal strain data. From the mechanics of materials, the three strain components of the finite element node  $\varepsilon_x, \varepsilon_y, \varepsilon_z$ , any positive strain at an angle to the x-axis of  $\alpha$  is calculated as:

$$\varepsilon_\alpha = \varepsilon_x \cos^2 \alpha + \varepsilon_y \sin^2 \alpha + \gamma_{xy} \sin \alpha \cos \alpha \tag{A7}$$

where  $\alpha$  is the strain bridge patch direction;  $\varepsilon_\alpha$  is the corresponding positive strain for the specified direction.

From Equation (A7), the response of the individual strain bridges that make up the Wheatstone strain bridge can be obtained as:

$$\begin{cases} \varepsilon_{Q1,Q3} = \varepsilon_{45^\circ} = (\varepsilon_x + \varepsilon_y + \gamma_{xy})/2 \\ \varepsilon_{Q2,Q4} = \varepsilon_{135^\circ} = (\varepsilon_x + \varepsilon_y - \gamma_{xy})/2 \end{cases} \tag{A8}$$

Substituting Equation (A8) into Equation (A1):

$$X_{sf} = 2\gamma_{xy} \tag{A9}$$

The method of deriving the relationship between the torque virtual strain bridge and the nodal strain follows the same process as that of the shear strain bridge, and it is sufficient to refer to the derivation process of the shear virtual strain bridge.

*Appendix A.2. Note 2 Original Samples from Virtual Calibration*

After completing the virtual ground calibration experiment, it is imperative to analyze the response of the strain gauges to ascertain their suitability for integration into the load equation. This analysis primarily involves evaluating the linearity, effectiveness, and sensitivity of the strain gauges. The strain data extracted from the wing finite element model for a load of 5 kN is presented in Table A1. The analysis of the selected strain gauge characteristics is depicted in Figure A1, illustrating that as the load level increases, the strain gauges demonstrate excellent linearity, effectiveness, and sensitivity.

**Table A1.** Strain data for a load of 5 kn.

| Load Level | M1 ( $\mu\varepsilon$ ) | M4 ( $\mu\varepsilon$ ) | Q11 ( $\mu\varepsilon$ ) | Q12 ( $\mu\varepsilon$ ) | Q22 ( $\mu\varepsilon$ ) | T11 ( $\mu\varepsilon$ ) | T12 ( $\mu\varepsilon$ ) | T22 ( $\mu\varepsilon$ ) |
|------------|-------------------------|-------------------------|--------------------------|--------------------------|--------------------------|--------------------------|--------------------------|--------------------------|
| 0          | 0                       | 0                       | 0                        | 0                        | 0                        | 0                        | 0                        | 0                        |
| 0.01       | 7.577                   | -7.577                  | 0.399                    | -0.897                   | -0.117                   | -6.854                   | 0.616                    | 2.005                    |
| 0.02       | 15.154                  | -15.153                 | 0.798                    | -1.795                   | -0.231                   | -13.706                  | 1.233                    | 4.012                    |
| 0.035      | 26.52                   | -26.517                 | 1.398                    | -3.14                    | -0.399                   | -23.979                  | 2.159                    | 7.026                    |
| 0.058      | 43.569                  | -43.563                 | 2.299                    | -5.159                   | -0.641                   | -39.376                  | 3.548                    | 11.557                   |
| 0.091      | 69.144                  | -69.128                 | 3.654                    | -8.188                   | -0.983                   | -62.445                  | 5.636                    | 18.376                   |
| 0.142      | 107.509                 | -107.469                | 5.694                    | -12.731                  | -1.449                   | -96.985                  | 8.776                    | 28.655                   |
| 0.218      | 165.06                  | -164.967                | 8.771                    | -19.548                  | -2.041                   | -148.646                 | 13.501                   | 44.193                   |

Table A1. Cont.

| Load Level | M1 ( $\mu\epsilon$ ) | M4 ( $\mu\epsilon$ ) | Q11 ( $\mu\epsilon$ ) | Q12 ( $\mu\epsilon$ ) | Q22 ( $\mu\epsilon$ ) | T11 ( $\mu\epsilon$ ) | T12 ( $\mu\epsilon$ ) | T22 ( $\mu\epsilon$ ) |
|------------|----------------------|----------------------|-----------------------|-----------------------|-----------------------|-----------------------|-----------------------|-----------------------|
| 0.332      | 251.392              | -251.177             | 13.426                | -29.78                | -2.684                | -225.769              | 20.63                 | 67.793                |
| 0.503      | 380.897              | -380.399             | 20.502                | -45.154               | -3.077                | -340.497              | 31.417                | 103.936               |
| 0.759      | 575.149              | -573.983             | 31.341                | -68.306               | -2.252                | -509.884              | 47.825                | 160.178               |
| 1          | 757.888              | -755.784             | 41.835                | -90.242               | 0.386                 | -665.208              | 63.515                | 215.963               |

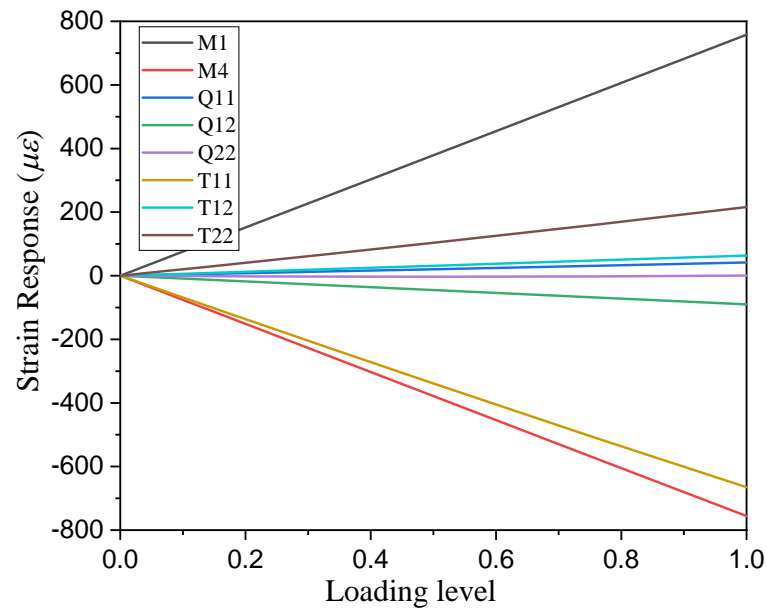


Figure A1. The characteristic analysis of strain gauge bridge.

Appendix A.3. Note 3 The Settings of All Deep Learning Models Used in This Paper

The models are constructed by Python code. The following functions involved are all from publicly available Python libraries.

Table A2. The Settings of Autoencoder Model Parameters.

| Input Layer   | Encoder Layer | Decoder Layer | Activation Function | Loss Function | Optimizer      | Training Epochs | Batch Size |
|---------------|---------------|---------------|---------------------|---------------|----------------|-----------------|------------|
| 18 dimensions | 13 neurons    | 18 neurons    | ReLU                | MSE           | Adam optimizer | 200             | 32         |

Table A3. The Settings of Locally LLE Model.

| Input Data    | Target Dimensionality | Test Set Size | Random Seed | Loss Function | Linear Regression Model |
|---------------|-----------------------|---------------|-------------|---------------|-------------------------|
| 18 dimensions | 13 components         | 50%           | 42          | MSE           | Linear Regression       |

Table A4. PCA Model Parameters.

| Input Data    | Target Dimensionality | Test Set Size | Random Seed | Loss Function |
|---------------|-----------------------|---------------|-------------|---------------|
| 18 dimensions | 13 components         | 50%           | 42          | MSE           |

**Table A5.** The Settings of RNN Model Parameters.

| Input Data    | Simple RNN Layer | Activation Function | Loss Function | Validation Sets | Training Epochs | Batch Size |
|---------------|------------------|---------------------|---------------|-----------------|-----------------|------------|
| 13 dimensions | 50 neurons       | ReLU                | MSE           | 20%             | 50              | 32         |

**Table A6.** The Settings of LSTM Model Parameters.

| Input Data    | LSTM Layer | Activation Function | Loss Function | Validation Sets | Training Epochs | Batch Size |
|---------------|------------|---------------------|---------------|-----------------|-----------------|------------|
| 13 dimensions | 50 neurons | ReLU                | MSE           | 20%             | 50              | 32         |

## References

- Zhou, L.; Li, X.; Li, M.; Żur, K.K. The smoothed finite element method for time-dependent mechanical responses of MEE materials and structures around Curie temperature. *Comput. Methods Appl. Mech. Eng.* **2020**, *370*, 113241. [CrossRef]
- Hughes, A.J.; Barthorpe, R.J.; Dervilis, N.; Farrar, C.R.; Worden, K. A probabilistic risk-based decision framework for structural health monitoring. *Mech. Syst. Signal Process.* **2021**, *150*, 107339. [CrossRef]
- Vinogradov, Y.I.; Menkov, G.B. Study of Stress-Strain State of an Aircraft Body at Steering Loads. *Mech. Solids* **2020**, *55*, 423–436. [CrossRef]
- He, H.; Zeng, B.; Wu, X.; Hou, J.; Wang, Y.; Wang, Y.; Wang, N. Higher matrix stiffness promotes VSMC senescence by affecting mi-tochondria-ER contact sites and mitochondria/ER dysfunction. *FASEB J.* **2023**, *37*, e23318. [CrossRef] [PubMed]
- Brown, E.R.; McCollom, N.N.; Moore, E.E.; Hess, A. Prognostics and Health Management—A data-driven approach to supporting the F-35 Lightning II. In Proceedings of the 2007 IEEE Aerospace Conference, Big Sky, MT, USA, 3–10 March 2007.
- Davies, A. Global Defense Procurement and the F-35 Joint Strike Fighter. *Secur. Chall.* **2019**, *15*, 79–81.
- Lei, W.Y.; Turkiyyah, G.; Knio, O. Finite Element Discretizations for Variable-Order Fractional Diffusion Problems. *J. Sci. Comput.* **2023**, *97*, 5. [CrossRef]
- Hu, Y.; Li, Y.; Yan, D.; Jiao, Z.; Yuan, D.; Qin, C.; Li, Y. Strain transfer of fiber Bragg grating sensors in fiber-reinforced polymer composites with different fiber orientations and temperatures. *Measurement* **2024**, *225*, 114005. [CrossRef]
- Duncan, J.S. *Pilot's Handbook of Aeronautical Knowledge*; United States Department of Transportation, Federal Aviation Administration, Airman Testing Standards Branch: Oklahoma City, OK, USA, 2016.
- Li, L.; Zhang, X.; Qian, C.; Wang, R. Basic flight maneuver generation of fixed-wing plane based on proximal policy optimization. *Neural Comput. Appl.* **2023**, *35*, 10239–10255. [CrossRef]
- Yang, J.F.; Zhang, N.; He, Y.L.; Zhu, Q.X.; Xu, Y. Novel dual-network autoencoder based adversarial domain adaptation with Wasserstein divergence for fault diagnosis of unlabeled data. *Expert. Syst. Appl.* **2024**, *238*, 122393. [CrossRef]
- Jeong, S.H.; Lee, K.B.; Ham, J.H.; Kim, J.H.; Cho, J.Y. Estimation of maximum strains and loads in aircraft landing using artificial neural network. *Int. J. Aeronaut. Space Sci.* **2020**, *21*, 117–132. [CrossRef]
- Hou, C.K.J.; Behdinan, K. Neural Networks with Input Dimensionality Reduction for Efficient Temperature Distribution Prediction in a Warm Stamping Process. *J. Appl. Comput. Mech.* **2022**, *8*, 1431–1444. [CrossRef]
- Gandy, M.; Martin, L. Wireless Sensors for Aging Aircraft Health Monitoring. Lockheed Martin Internal Document, 2000. Available online: [https://my.ece.utah.edu/~cfurse/Center%20of%20Excellence/wiring\\_papers/wireless\\_sensors\\_for\\_ag\\_2001.pdf](https://my.ece.utah.edu/~cfurse/Center%20of%20Excellence/wiring_papers/wireless_sensors_for_ag_2001.pdf) (accessed on 1 March 2024).
- Silva, G.N.; Sant'Anna, I.C.; Cruz, C.D.; Nascimento, M.; Azevedo, C.F.; Glória, L.S. Neural networks and dimensionality reduction to increase predictive efficiency for complex traits. *Genet. Mol. Res.* **2022**, *21*, gmr18982. [CrossRef]
- Bucci, A.; He, L.D.; Liu, Z. Combining dimensionality reduction methods with neural networks for realized volatility forecasting. *Ann. Oper. Res.* **2023**. [CrossRef]
- Mendez, M.A. Linear and nonlinear dimensionality reduction from fluid mechanics to machine learning. *Meas. Sci. Technol.* **2023**, *34*, 042001. [CrossRef]
- Nateghi, V.; Manzi, M. Machine learning methods for nonlinear dimensionality reduction of the thermospheric density field. *Adv. Space Res.* **2023**, *72*, 4106–4114. [CrossRef]
- Bunnell, S.; Gorrell, S.; Salmon, J.; Thelin, C.; Ruoti, C. Structural design space exploration using principal component analysis. *J. Comput. Inf. Sci. Eng.* **2020**, *20*, 061014. [CrossRef]
- Rahbari, A.; Rébillat, M.; Mechbal, N.; Canu, S. Unsupervised damage clustering in complex aeronautical composite structures monitored by Lamb waves: An inductive approach. *Eng. Appl. Artif. Intell.* **2021**, *97*, 104099. [CrossRef]
- Shitomi, R.; Tsuji, M.; Fujimura, Y.; Funatomi, T.; Mukaigawa, Y.; Morimoto, T.; Oishi, T.; Takamatsu, J.; Ikeuchi, K. Unsupervised learning with a physics-based autoencoder for estimating the thickness and mixing ratio of pigments. *J. Opt. Soc. Am. A* **2023**, *40*, 116–128. [CrossRef] [PubMed]

22. Liu, Z.B.; Liu, F.J.; Wang, Y.C.; Zhang, Y.L.; Sun, Z.X.; Zhang, M.S. Prediction of retaining structure deformation of ultra-deep foundation pit by empirical mode decomposition with recurrent neural networks. *Environ. Earth Sci.* **2023**, *82*, 553. [[CrossRef](#)]
23. Erol, B.; Inkaya, T. Long short-term memory network based deep transfer learning approach for sales forecasting. *J. Fac. Eng. Arch. Gaz.* **2024**, *39*, 191–202. [[CrossRef](#)]
24. Bärmann, A.; Burlacu, R.; Hager, L.; Kutzer, K. An Approximation Algorithm for Optimal Piecewise Linear Interpolations of Bounded Variable Products. *J. Optim. Theory Appl.* **2023**, *199*, 569–599. [[CrossRef](#)]
25. Thiam, A.; Baratoux, D.; Fall, M.; Faye, G.; Ouattara, G. Multi-Parameter Statistical Analysis of K, Th, and U Concentrations in Eastern Senegal: Implications for the Interpretation of Airborne Radiometrics. *Geosciences* **2023**, *13*, 263. [[CrossRef](#)]
26. Zhang, M.; Xia, S.; Huang, Y.; Tian, J.; Yin, Z. Research on Engine Thrust and Load Factor Prediction by Novel Flight Maneuver Recognition Based on Flight Test Data. *Aerospace* **2023**, *10*, 961. [[CrossRef](#)]
27. Korada, V.S.; Kumar, J. Finite elements limit analysis formulation using the power type yield criterion for plane strain and axisymmetric stability problems. *Comput. Geotech.* **2023**, *162*, 105667. [[CrossRef](#)]
28. Elakkiya, M.K. Novel deep learning models with novel integrated activation functions for autism screening: AutoNet and MinAutoNet. *Expert. Syst. Appl.* **2024**, *238*, 122102. [[CrossRef](#)]
29. Zhao, Y.; Wang, Y.C.; Hao, J.B.; Wang, Y.Q.; Wang, K.C.; Tai, S.Y. Study on mechanical properties of cellular structures with negative Poisson's ratio based on the development of Abaqus plug-in tool. *Compos. Struct.* **2023**, *322*, 117348. [[CrossRef](#)]

**Disclaimer/Publisher's Note:** The statements, opinions and data contained in all publications are solely those of the individual author(s) and contributor(s) and not of MDPI and/or the editor(s). MDPI and/or the editor(s) disclaim responsibility for any injury to people or property resulting from any ideas, methods, instructions or products referred to in the content.